









Cite this: *Energy Environ. Sci.*,  
2024, 17, 5490

# Precise control of process parameters for >23% efficiency perovskite solar cells in ambient air using an automated device acceleration platform†

Jiyun Zhang, \*<sup>ab</sup> Jianchang Wu,<sup>ab</sup> Anastasia Barabash,<sup>b</sup> Tian Du,<sup>ab</sup> Shudi Qiu, <sup>b</sup> Vincent M. Le Corre, <sup>ab</sup> Yicheng Zhao,<sup>c</sup> Kaicheng Zhang, <sup>b</sup> Frederik Schmitt, <sup>a</sup> Zijian Peng, <sup>b</sup> Jingjing Tian,<sup>b</sup> Chaohui Li, <sup>b</sup> Chao Liu,<sup>ab</sup> Thomas Heumueller, <sup>ab</sup> Larry Lüer,<sup>b</sup> Jens A. Hauch<sup>ab</sup> and Christoph J. Brabec\*<sup>ab</sup>

Achieving high-performance perovskite photovoltaics, especially in ambient air, is critically dependent on the precise optimization of process parameters. However, traditional manual methods often struggle to effectively control the key variables. This inherent challenge requires a paradigm shift toward automated platforms capable of precise and reproducible experiments. Herein, we use a fully automated device acceleration platform (DAP) to optimize air-processed parameters for preparing perovskite devices using a two-step sequential deposition technique. Over ten process parameters with significant potential to influence device performance are systematically optimized. Specifically, we delve into the impact of the dripping speed of organic ammonium halide, a parameter that is difficult to control manually, on both perovskite film and device performance. Through the targeted design of experiments, we reveal that the dripping speed significantly affects device performance primarily by adjusting the residual  $\text{PbI}_2$  content in the films. We find that optimal dripping speeds, such as  $50 \mu\text{L s}^{-1}$ , contribute to top-performance devices. Conversely, excessively fast or slow speeds result in devices with comparatively poorer performance and lower reproducibility. The optimized parameter set enables us to establish a standard operation procedure (SOP) for additive-free perovskite processing in ambient conditions, which yield devices with efficiencies surpassing 23%, satisfactory reproducibility, and state-of-the-art photo-thermal stability. This research underscores the importance of understanding the causality of process parameters in enhancing perovskite photovoltaic performance. Furthermore, our study highlights the pivotal role of automated platforms in discovering innovative workflows and accelerating the development of high-performing perovskite photovoltaic technologies.

Received 30th March 2024,  
Accepted 27th June 2024

DOI: 10.1039/d4ee01432d

rsc.li/ees

## Broader context

The rapid advancement of emerging perovskite photovoltaic (PV) technology is a beacon of hope in the quest for efficient and cost-effective energy solutions. With the efficiency of perovskite-based devices soaring, the conventional fabrication process, confined to inert atmospheres (e.g.,  $\text{N}_2$ -filled glovebox), poses significant hurdles for large-scale production and cost reduction. The necessity to shift towards air-based fabrication methods is palpable. However, the journey is fraught with challenges, particularly the precise control of critical process variables, and is often hampered by the limitations of manual optimization reliant on operator expertise. Here, we introduce an air-based perovskite devices manufacturing protocol, which harnesses the potential of an automated device acceleration platform (DAP) to transcend the constraints of traditional methods. By leveraging the automation platform, we embark on a methodical exploration of process parameters, culminating in the optimization of fabrication technique that yields high-efficiency additive-free perovskite devices with exceptional reproducibility and stability under ambient conditions.

<sup>a</sup> Forschungszentrum Jülich GmbH, Helmholtz-Institute Erlangen-Nürnberg (HI ERN), Department of High Throughput Methods in Photovoltaics, Immerwahrstraße 2, Erlangen 91058, Germany

<sup>b</sup> Friedrich-Alexander-University Erlangen-Nuremberg (FAU), Faculty of Engineering, Department of Material Science, Institute of Materials for Electronics and Energy Technology (i-MEET), Martensstrasse 7, Erlangen 91058, Germany. E-mail: jiyun.zhang@fau.de, christoph.brabec@fau.de

<sup>c</sup> University of Electronic Science and Technology of China (UESTC), State Key Laboratory of Electronic Thin Films and Integrated Devices, School of Electronic Science and Engineering, Chengdu 611731, China

† Electronic supplementary information (ESI) available: Supplementary information includes the Experimental section, Fig. S1–S25, Table S1, and a Supplemental Video. See DOI: <https://doi.org/10.1039/d4ee01432d>



## Introduction

Emerging perovskite photovoltaics have become a revolutionary next-generation technology in the renewable energy field, providing unprecedented opportunities for efficient and affordable solar power generation.<sup>1–3</sup> At the core of this advancement is the pursuit of high-performance perovskite photovoltaic technology, which is essential to unlock the full potential and maximize the capabilities of this promising technology.<sup>4,5</sup> The fabrication of high-performance perovskite devices usually requires an inert atmosphere (for instance a nitrogen-filled glovebox),<sup>6,7</sup> which dramatically reduces scalability due to higher preparation costs, limited production scale, and more complicated preparation processes.<sup>8,9</sup> Therefore, the preparation of high-performance perovskite solar cells (PSCs) in ambient air is expected to overcome these challenges. The realization of high-performance PSCs in ambient air is closely related to the precise control and optimization of various manufacturing process parameters that govern the quality of the perovskite film and device fabrication.<sup>10,11</sup> Hence, the optimal selection of process parameters has become a key factor affecting the efficiency and stability of perovskite photovoltaic cells.<sup>12</sup>

However, traditional manual methods encounter huge challenges in effectively controlling key variables as they are frequently limited by the skills and experience of the operators.<sup>13,14</sup> These challenges are exacerbated by the rapid crystallization dynamics of perovskites, significantly adding complexity to the fabrication process in addition to the intricate interdependence of factors affecting device performance. As nucleation and crystal growth occur on the sub-second timescale and strongly depend on preconditions (e.g., solvent-/gas-quenching), manual operations are finding their limits in achieving highly reproducible outcomes upon mass production.<sup>15,16</sup> To overcome the limitations of manual optimization methods and unlock the full potential of perovskite photovoltaics fabricated in ambient air, there is an increasingly urgent need for a paradigm shift toward innovative technologies that enable more precise and reproducible experiments.

Automated material and device acceleration platforms (MAPs and DAPs) have emerged as transformative tools across various scientific fields, promoting breakthroughs and efficiency improvements through high-throughput experiments and systematic exploration.<sup>17–21</sup> The main advantage of these automated platforms is their capability to perform experiments with unprecedented efficiency and reproducibility.<sup>22</sup> By automating repetitive tasks and minimizing human intervention, these platforms ensure a FAIR data integrity as well as the highest reliability.<sup>23–25</sup> With exceptional precision, speed, and accuracy, automated platforms have achieved remarkable success in accelerating research in areas like organic synthesis, drug discovery, and biology technology.<sup>26–31</sup> The methodology of integrating automation in energy thin film materials research, especially solution-processed perovskite photovoltaics materials, has attracted widespread attention.<sup>10,32–36</sup> Compared to traditional manual methods, DAPs are specifically promising

for perovskite photovoltaics manufacturing where rather small inconsistencies in the process can cause significant deviation in the batch-to-batch performance.<sup>37</sup> We believe that the introduction of automated manufacturing systems in perovskite photovoltaics research holds great potential for overcoming long-standing challenges associated with manual manufacturing methods.

In this study, we utilize an automated DAP named SPINBOT to optimize process parameters for fabricating full perovskite devices in ambient air. The process parameters that significantly affect device performance were systematically optimized using the one-variable-at-a-time (OVAT) method. Specifically, the influence of the dripping speed of organic ammonium halide on both perovskite film and device performance was finely studied. The results demonstrate that moderate dripping speeds (e.g., 50  $\mu\text{L s}^{-1}$ ) are most advisable for producing top-performing devices, whereas too fast or slow speeds would result in samples with relatively poorer performance and uneven outcomes. By optimizing the parameter set, we finally achieved perovskite devices processed under ambient conditions with a champion efficiency exceeding 23%. Furthermore, the devices from optimized parameters demonstrated excellent reproducibility and state-of-the-art photo-thermal stability, retaining  $93\% \pm 3\%$  of their initial efficiency after 1200 hours of continuous aging. This study highlights not only the significance of precise process parameter optimization for enhancing perovskite photovoltaic performance but also demonstrates the critical role of automated platforms in streamlining experimental workflows and accelerating high-performance perovskite photovoltaics development.

## Results and discussion

Fig. 1A illustrates the automated fabrication procedure for solution-processed PSCs with a structure of ITO/SnO<sub>2</sub>/Perovskite/Spiro-OMeTAD/Au (Fig. 1B) using the two-step sequential deposition technique in ambient air. Specifically, a wet PbI<sub>2</sub>/CsI layer is formed by depositing the PbI<sub>2</sub>/CsI precursor onto a SnO<sub>2</sub>-coated ITO substrate without annealing.<sup>38</sup> In the next step, the organic ammonium halide solution is dynamically drop-cast onto the wet PbI<sub>2</sub>/CsI film. After spin-drying the layer, the substrate is then annealed in the air. The final spin-coating step involves the deposition of spiro-OMeTAD solution as the hole-transporting layer. All the above solution-processed layers are formed through the SPINBOT platform in the air environment. The streamlined fabrication process of thin layers can be found in the ESI† Video.

To evaluate the influence of process parameters on device performance, a comprehensive parameter list of all process parameters was first compiled, as illustrated in Fig. S1 (ESI†). Based on the preliminary review and analysis of various process parameters that potentially affect device performance, over ten individual and combination parameters, such as operational conditions, precursor volumes (Fig. S2, ESI†), spin speed combinations (Fig. S3, ESI†) and spin duration at different stages



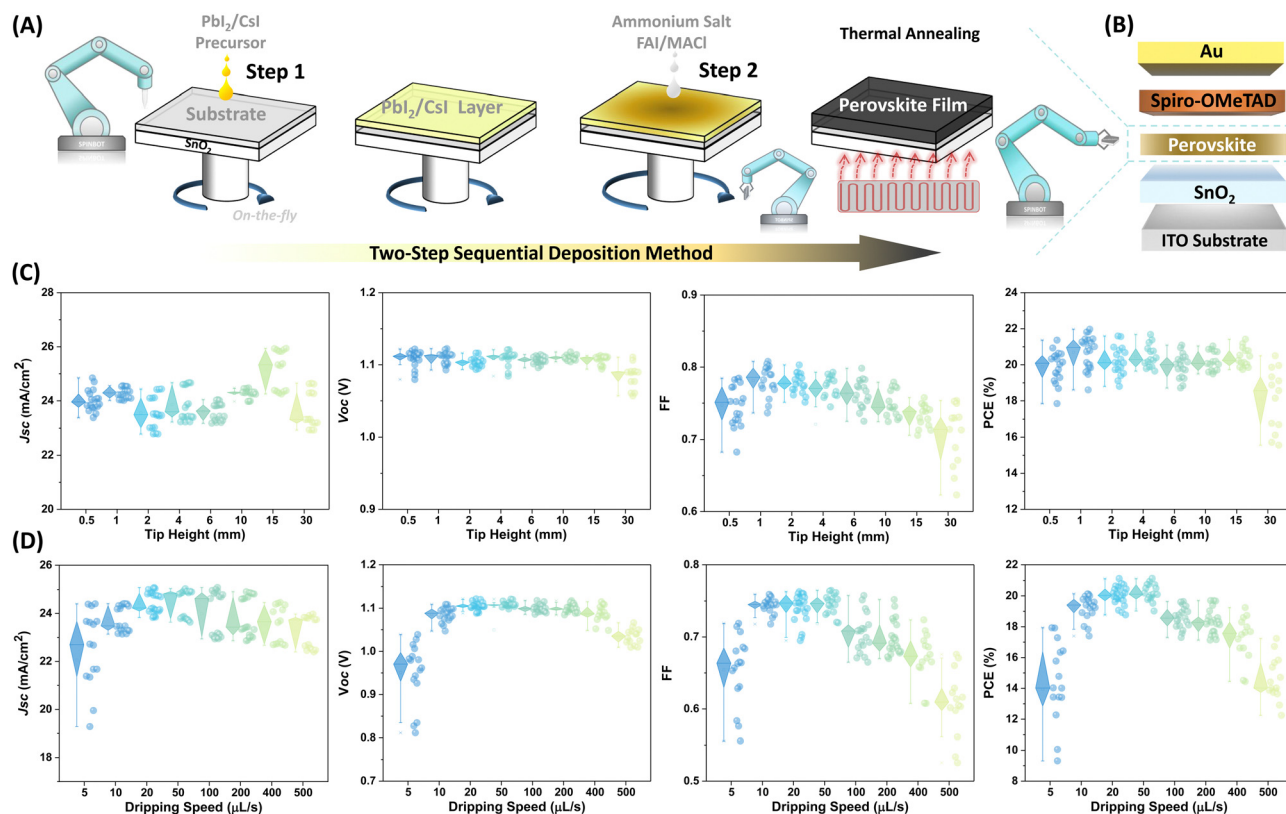


**Fig. 1** Schematic of automated fabrication and statistical performance of perovskite devices. (A) Schematic of the autonomous fabrication process for perovskite films using the two-step sequential deposition method. (B) The architecture of PSCs (ITO/SnO<sub>2</sub>/perovskite/Spiro-OMeTAD/Au). (C) Grouped performance statistics for perovskite devices fabricated with different pipette tip heights at the drip of FAI/MACI solution. The tip heights are 0.5, 1, 2, 4, 6, 10, 15, and 30 mm, respectively. (D) Statistical performance of the perovskite devices as a function of the dripping speed of the ammonium halide. The drip speeds are 5, 10, 20, 50, 100, 200, 400, and 500  $\mu\text{L s}^{-1}$ , respectively.

**Table 1** The input variables and their potential impact on device performance

Input variable	Range (min–max)	Interval	Relative efficiency potential	Potential factor
Atmosphere (gas flow)	0–5 bar	1 bar	9.0–75.2%	0.662
Spin speed S1	900–2500 rpm	200 rpm	43.0–93.9%	0.509
Spin speed S2	900–2500 rpm	250 rpm	43.0–93.9%	0.509
Spin duration $t_2$	12–21 s	3 s	66.2–96.1%	0.299
Pipette tip height	0.5–30 mm	1 mm	169.8–98.7%	0.289
Dripping speed	5–500 $\mu\text{L s}^{-1}$	5 $\mu\text{L s}^{-1}$	30.6–94.8%	0.642
Spin duration $t_3$	5–26 s	3 s	71.1–100%	0.289
Spiro-OMeTAD	Static/OTF (on-the-fly)		82.1–92.8%	0.107
Dispense mode	Dynamic		77.4–91.1%	0.137
Spin speed S3	3000–5000 rpm	1000 rpm	58.0–76.7%	0.187

(Fig. S4 and S5, ESI<sup>†</sup>), were selected for in-depth study, as listed in Table 1. The process parameters were identified and optimized using the OVAT method. This approach allowed us to effectively isolate and analyze the impact of each parameter. To quantify the impact of individual process parameters on device performance, particularly efficiency, we introduced two indicators: relative efficiency potential and potential factor. Relative efficiency potential is defined as the normalized range of change in device efficiency from the minimum to the maximum within a given parameter optimization range. The potential factor further quantifies this change interval and is represented by calculating the difference between the

minimum and maximum values of the normalized efficiency. This method allowed us to intuitively identify and evaluate the impact intensity of individual process parameters on device performance, thus revealing the key parameters that influence the final performance of the device. After experimental research and data analysis, the operational atmosphere, spin speed combinations, pipette tip height, and dripping speed of organic ammonium salt were identified as key parameters that significantly impact device performance. In the following section, their effects on the device/film are detailed.

In the SPINBOT system, nitrogen gas flow is normally supplied into the mini-spin-coater bowl (Fig. S6, ESI<sup>†</sup>) for



rapid removal of residual solvent vapor and the creation of a better-controlled atmosphere during the film deposition process.<sup>39</sup> To investigate the influence of operational conditions on the device performance, different operational atmospheres were built by adjusting the airflow pressure. Fig. S7 (ESI†) presents the statistical performance distribution of perovskite devices fabricated under different operational atmospheres. The impact of nitrogen supply on device performance is evident. Samples processed without gas flow exhibit the poorest performance, with efficiencies ranging between 2–5%. This indicates that unregulated solvent accumulation within the spin-coater can dramatically impair the device's performance. However, there is a remarkable improvement in device performance with the introduction of fresh airflow. In particular, when the airflow pressure was set to 3 bar, the efficiency and uniformity of the devices reached the optimum level compared to other conditions. A notable advantage of the SPINBOT platform over manual process engineering is its capability to control typically unregulated parameters, such as the pipette tip height and ejection speed of the spin-coating dripping nozzle. Fig. 1C presents the grouped statistics illustrating the impact of various pipette tip heights during FAI/MACl dripping on the performance metrics of perovskite devices. The results suggest that relatively lower tip heights generally enhance the fill factor (FF) and PCE, while the short-circuit current density ( $J_{sc}$ ) and open-circuit voltage ( $V_{oc}$ ) are less sensitive to changes in tip height. Specifically,  $V_{oc}$  values remain relatively stable across a range of tip heights, which only show minor fluctuations at the maximum height of 30 mm. FF improves slightly as the tip height increases from 0.5 to 2 mm, then plateaus and gradually declines with further increases in tip height. Devices with a tip height of 30 mm exhibit significantly poorer performance and reproducibility, indicating that tip heights exceeding 15 mm during ammonium halide solution dripping can significantly impair device performance.  $J_{sc}$  values are relatively constant across varying tip heights, with a slight increase observed at higher heights. PCE improves markedly at a tip height of 1–2 mm, but efficiency gains level off or decrease slightly beyond this range. The optimal PCE is observed at a tip height of 1 mm, underscoring the importance of maintaining relatively lower tip heights during FAI/MACl dripping to achieve optimal device performance. Another critical parameter, the dripping speed of organic ammonium halide precursor, which was often overlooked in previous literature due to the huge challenges of manual control, can be more precisely regulated with the robotic platform. By fixing the dripping volume of the ammonium halide solution and varying the dripping speed in increments as small as  $0.1 \mu\text{L s}^{-1}$  (ranging from  $0.1$  to  $500 \mu\text{L s}^{-1}$ ), we were able to thoroughly investigate this aspect in perovskite processing. Here, the dripping speed refers to the ejection speed at which the ammonium halide solution is dispensed from the pipette tip onto the preformed  $\text{PbI}_2/\text{CsI}$  layer during the spin-coating process. Fig. 1D presents the statistical performance distribution of perovskite devices as a function of ejection speeds (5, 10, 20, 50, 100, 200, 400, and  $500 \mu\text{L s}^{-1}$ , respectively) of ammonium halide. It is obvious that

this parameter massively influences the performance behavior of the resulting devices, particularly the  $J_{sc}$  and FF. Generally, these performance metrics improve as the speed increases, but they gradually decline after reaching an optimum of around  $20$  to  $50 \mu\text{L s}^{-1}$  with further acceleration. Deviations from this optimal range, either too fast or too slow speeds can lead to devices with relatively poorer performance and uncertain outcomes.

To investigate the underlying mechanism behind this phenomenon, the microstructural features of the films were first examined. Top-view scanning electron microscope (SEM) images in Fig. 2A and Fig. S8 and S9 (ESI†) illustrate the morphological variations observed in perovskite thin films. While all samples display compact and pinhole-free characteristics, noticeable differences in morphology are observed. The grain size distributions depicted in Fig. S10 (ESI†) demonstrate that increasing dripping speeds are correlated with noticeable increases in grain sizes. Specifically, the grain size averages are as follows: at a dripping speed of  $5 \mu\text{L s}^{-1}$ , the grains measure approximately  $1.01 \mu\text{m}$ ; increasing the speeds to  $50$  and  $200 \mu\text{L s}^{-1}$  results in an average size of  $1.3$  and  $1.81 \mu\text{m}$ , respectively; and at the highest speed of  $500 \mu\text{L s}^{-1}$ , the grains average  $2.3 \mu\text{m}$ . Additionally, as the dripping speeds increase, there is a noticeable increase in the content of the white phase. Remarkably, when the speed exceeds  $400 \mu\text{L s}^{-1}$ , approximately half of the film surface is occupied by the white phase. Previous studies have linked the white phase to the  $\text{PbI}_2$  phase, while the black phases are associated with perovskite materials, indicating the predominant presence of the  $\text{PbI}_2$  phase along the grain boundaries of perovskites.<sup>40</sup> This observation is further confirmed by X-ray diffraction (XRD) patterns presented in Fig. 2B, which demonstrate an escalating diffraction intensity of the  $\text{PbI}_2$  phase at  $12.7^\circ$  with higher dripping speeds. Conversely, the diffraction intensity of the primary perovskite phases around  $14.0^\circ$  exhibits an almost linear increase, reaching peak values within the speed range of  $50$  to  $200 \mu\text{L s}^{-1}$ , beyond which it declines with the further acceleration of the ejection speed, as depicted in Fig. 2C. Dripping speed markedly influences the thickness of the resulting films (Fig. S11, ESI†). As the dripping speed increases, there is a corresponding decrease in film thickness, ranging from approximately  $860 \text{ nm}$  to about  $800 \text{ nm}$ . Notably, this variation in thickness is more pronounced at relatively higher and lower dripping speeds.

Driven by the significant impact of dripping speed on perovskite film and device performance, we further reduced the dripping speed to observe the resultant effects. As shown in Fig. S12 (ESI†), as the speeds decrease from  $10 \mu\text{L s}^{-1}$  to  $5, 4, 2, 1,$  and  $0.5 \mu\text{L s}^{-1}$ , the colors of samples change from completely black to yellowish during spin coating and the samples processed with slow dripping speeds cannot convert to black perovskite phase even after thermal annealing (Fig. 2D). The appearance of yellow phases at the film edges is observed at a speed of  $5 \mu\text{L s}^{-1}$ , their proportion increases at  $4 \mu\text{L s}^{-1}$  ultimately resulting in a yellowish film at speeds below  $2 \mu\text{L s}^{-1}$ . These yellow non-perovskite phases are identified as  $\text{PbI}_2$ -DMSO compounds through structural and *in situ* optoelectronic characterization (Fig. S13, ESI†).<sup>41</sup> The lower ejection



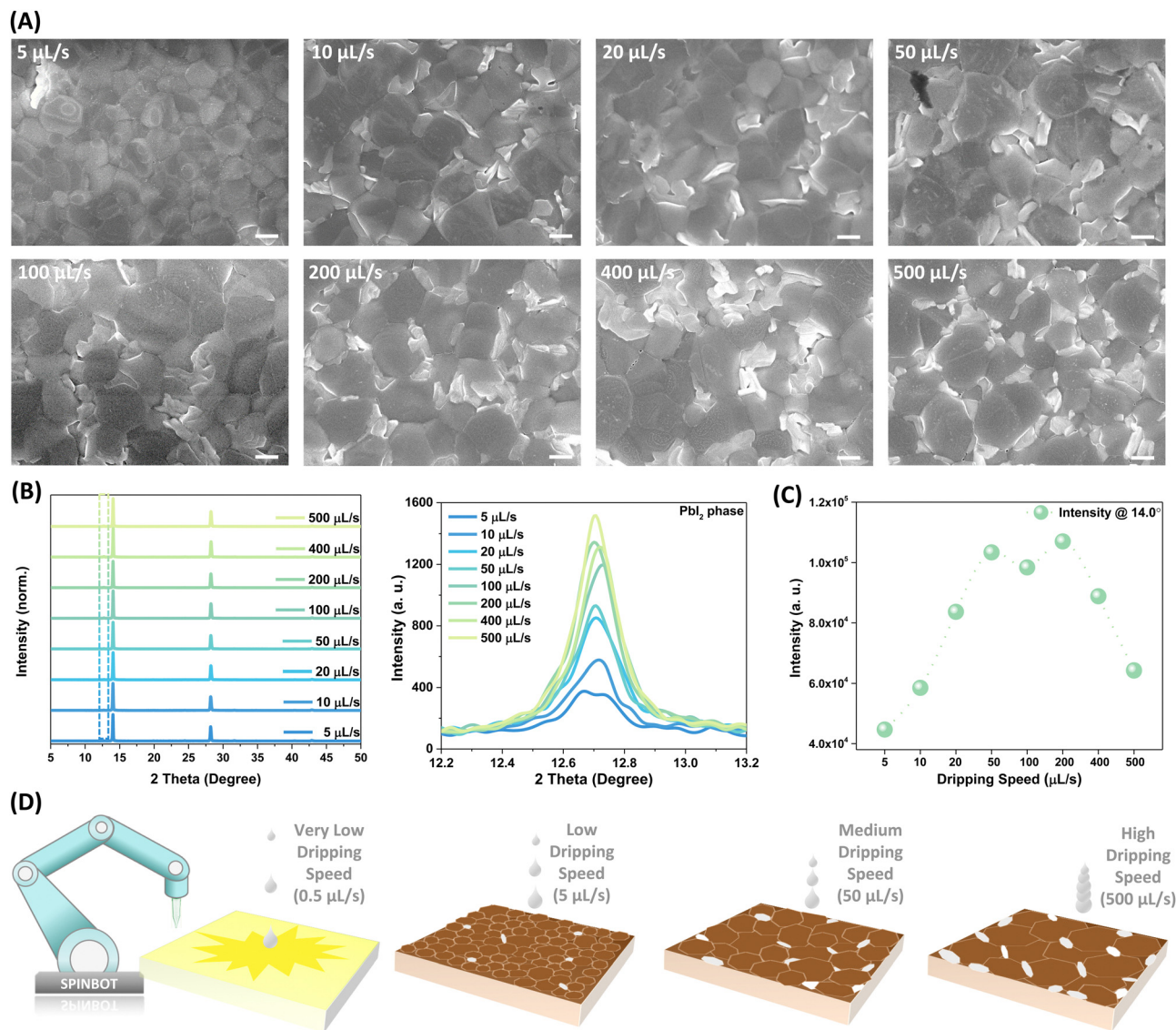


Fig. 2 Structural characterizations and analysis of perovskite thin films. (A) Top-view SEM images (the scale bar is 1  $\mu\text{m}$ ), (B) XRD patterns and magnified view focused around  $12.7^\circ$  (corresponds to  $\text{PbI}_2$  phase), and (C) diffraction intensity of perovskite phase peaks (at  $14^\circ$ ) of perovskite films fabricated with different dripping speeds of organic ammonium halide solution. (D) Schematic of the effect of varying dripping speeds on the morphology and crystallization of perovskite films.

speed leads to a prolonged dripping interval. For example, at a speed of  $2 \mu\text{L s}^{-1}$ , dispensing a droplet of isopropanol (IPA) based precursor (approximately 6–7  $\mu\text{L}$ ) results in an interval of approximately 3–3.5 s. This extended duration poses challenges for the ammonium salts dissolved in volatile IPA solvent to quickly replace the DMSO molecules intercalated in the  $\text{PbI}_2$  phase beneath the surface through direct intramolecular exchange, while converting the perovskite partially on the top, thus hindering the complete generation of perovskite crystallization.<sup>42</sup> The results indicate a critical minimum dripping speed for ammonium halide necessary for complete perovskite formation when employing the two-step deposition method (Fig. S14, ESI<sup>†</sup>). In our experiments, this threshold dripping speed is approximately  $10 \mu\text{L s}^{-1}$  (the dripping interval is about 0.6 s).

The structural variations within the perovskite lattice result in diverse optoelectronic properties. Notably, the solution dripping speed significantly influences the bandgap and homogeneity of the films. As presented in Fig. 3A and Fig. S15 (ESI<sup>†</sup>), the sample prepared with the lowest dripping speed exhibits the smallest bandgap ( $\sim 1.55 \text{ eV}$ ), with the peaks gradually shifting towards a wider direction from 800.9 nm to 794.3 nm. The optical bandgap of  $\text{PbI}_2$  is larger than that of perovskite, which may cause the blue shift of the PL emission peak.<sup>43</sup>  $\text{PbI}_2$  can form a type-I band alignment with perovskite,<sup>44,45</sup> and excess  $\text{PbI}_2$  can passivate the surface or/and grain boundary of perovskite layers, which can enhance solar cell performance, particularly in terms of charge separation and collection.<sup>46–48</sup> To evaluate film homogeneity, multiple positions (13 points) with regular patterns on each sample were characterized through a



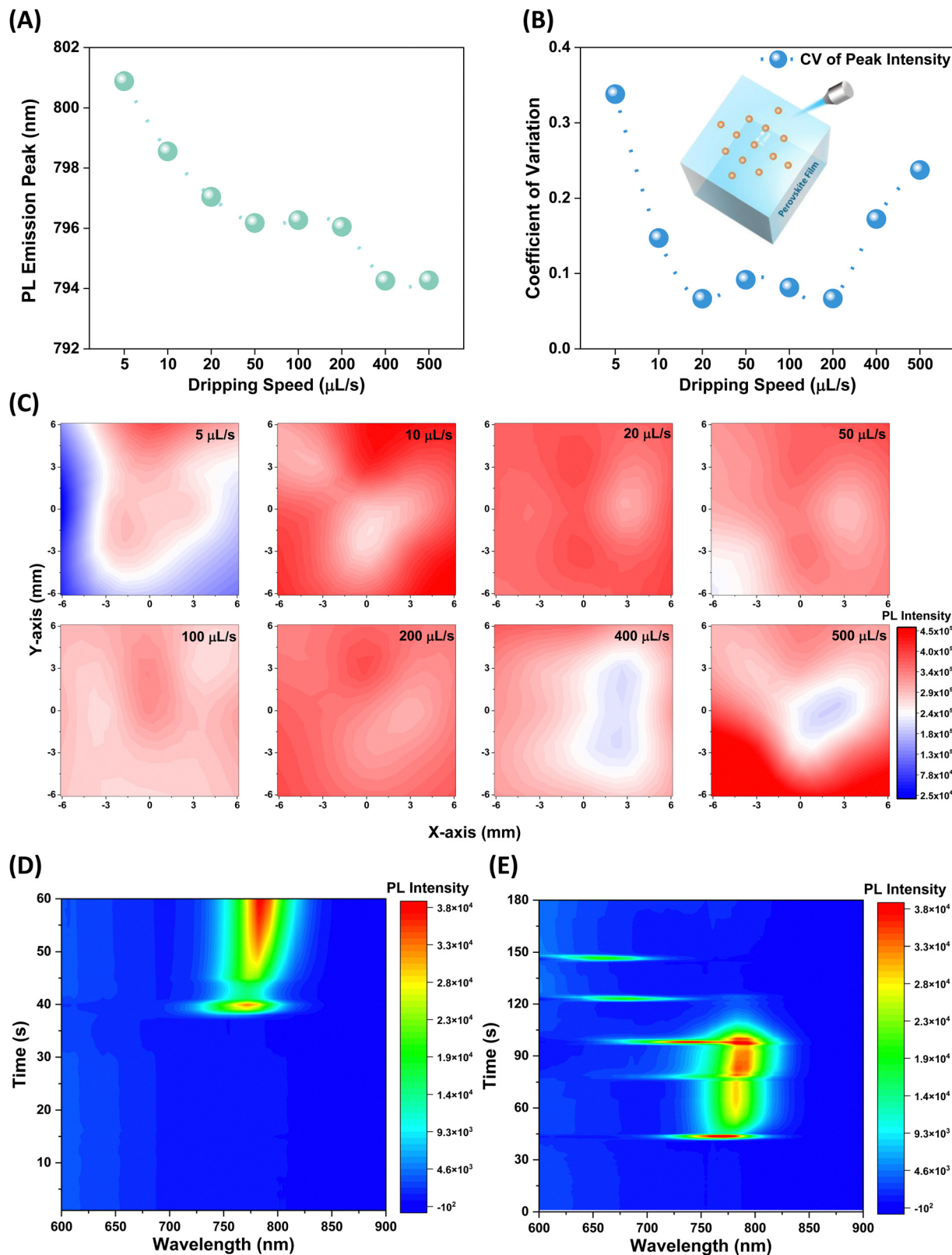


Fig. 3 Optoelectronic properties of perovskite thin films. (A) PL emission peaks, (B) coefficient variation of PL peaks intensity, and (C) PL intensity contour map for perovskite films prepared with varying dripping speeds of ammonium halide precursor. The PL mapping figures are plotted as value maps of slices, with 13 specific points in each film collected. *In situ* PL spectra of wet perovskite films fabricated with (D) fast ( $> 50 \mu\text{L s}^{-1}$ ) and (E) slow ( $\sim 0.5 \mu\text{L s}^{-1}$ ) dripping speeds of FAI/MACl solution. The PL signals were collected during the spin-coating process.



high-throughput spectrometer.<sup>49–51</sup> The coefficient of variation (CV) of PL peak intensity extracted from these PL spectra (Fig. S16, ESI†) was calculated, as depicted in Fig. 3B. The CV value gradually decreases at a doubling rate as the ejection speeds increase (indicating better homogeneity), and maintains a relatively lower value range between 20 to 200  $\mu\text{L s}^{-1}$ . Conversely, continuous increases in dripping speed lead to a rapid decrease in film uniformity. A similar trend is observed for samples fabricated with different dripping volumes of organic ammonium halide precursor (Fig. S17, ESI†). To visually depict the evolution of homogeneity in the samples, PL intensity contour maps were plotted and presented in Fig. 3C. It is evident that relatively lower or higher dripping speeds significantly compromise film homogeneity, while films with satisfactory homogeneity are achieved within the speed range of 20 to 200  $\mu\text{L s}^{-1}$ . The conclusion is further evidenced by the UV-Vis absorption spectra of films prepared at various speeds (Fig. S18, ESI†). Fig. 3D and E present the *in situ* PL spectra of wet perovskite films fabricated with fast ( $> 50 \mu\text{L s}^{-1}$ ) and slow ( $\sim 0.5 \mu\text{L s}^{-1}$ ) dripping speeds, respectively. Obviously, faster dripping speed facilitates the rapid formation of the perovskite phase, resulting in strong and continuous PL signals. In contrast, the film fabricated with relatively slower dripping speeds shows weaker perovskite signals, with emission signals that gradually blue-shifted and decreased in intensity. These observations indicate that the formation of non-perovskite phases at lower dripping speed and their subsequent conversion to

the perovskite phase is critically dependent on the dripping speed. The relatively faster speeds facilitate a more efficient and rapid phase transition (Fig. S19, ESI†). Hence, an optimal range of solution dripping speed is identified, enabling the fabrication of devices with high performance and homogeneity. It should be noted that the parameter optimization was not limited to the perovskite active layer but also the hole transport layer (Fig. S20, ESI†). By finely adjusting and optimizing each layer, we can significantly improve the optoelectronic performance of the devices.

Through careful optimization and regulation of each device preparation parameter, the overall performance of the devices is significantly enhanced compared to the initial samples. To further improve the device performance, a phenethylammonium iodide (PEAI) passivation layer was coated onto the perovskite surface (Fig. S21, ESI†).<sup>52</sup> Fig. 4A illustrates the  $J$ - $V$  curves of the best device after optimization. The optimized perovskite devices demonstrate outstanding performance, boasting a PCE of 23.1%, a  $J_{\text{sc}}$  of 25.4  $\text{mA cm}^{-2}$ , an open-circuit voltage ( $V_{\text{oc}}$ ) of 1.15 V, and a FF of 0.79. These metrics significantly surpass those of the best manually fabricated control group devices (Fig. S22, ESI†). As indicated by the external quantum efficiency (EQE) spectrum (Fig. 4B), the integrated current density is consistent with the value obtained from the  $J$ - $V$  curve with a slight deviation. The performance reproducibility was demonstrated through the repeated fabrication

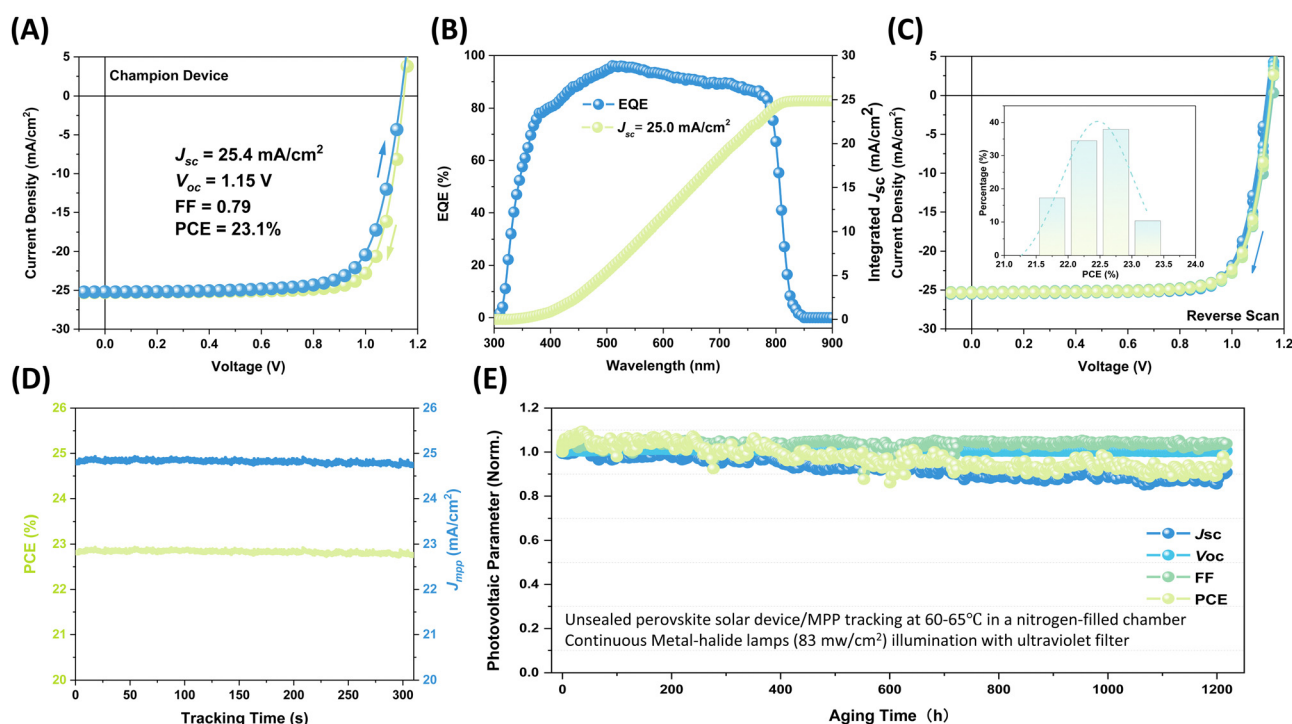


Fig. 4 Characterizations of the optimized devices. (A)  $J$ - $V$  curves of the champion device. Insert text provides the performance information. The spin speed combination is 1300 rpm  $\times$  1750 rpm, the dripping speed is 50  $\mu\text{L s}^{-1}$ . (B) EQE spectrum and integrated  $J_{\text{sc}}$  of the optimized devices. (C)  $J$ - $V$  curves and PCE distributions histogram (28 cells) for the devices fabricated with optimized parameters. (D) The MPP tracking of the unpacked device under simulated AM 1.5G illumination for approximately 300 s in ambient air with continuous nitrogen flow. The data is collected at  $J_{\text{mpp}}$  with a constant voltage ( $V_{\text{mpp}}$ ) of 0.908 V. (E) The results of the long-term stability test. The samples were tested at 60–65  $^{\circ}\text{C}$  in a nitrogen-filled chamber under continuous metal-halide lamp illumination (83  $\text{mW cm}^{-2}$ ) in reverse directions.



of devices with the optimized process parameters. The data in Fig. 4C demonstrate that these devices consistently achieve high performance with excellent reproducibility. The reproducibility and uniformity of device performance were further demonstrated by plotting the efficiency values histogram of 28 cells. The histogram shows that the efficiency values of most devices are concentrated within a relatively narrow range, without any noticeable outliers or irregular distributions. The performance of ambient-processed n-i-p devices prepared with/without additive engineering methods is summarized in Table S1 (ESI†). The data demonstrate that devices fabricated using the automated platform can achieve comparable or better performance. These results indicate that the optimized fabrication process is reliable and capable of producing devices with high consistency and uniformity.

With the satisfactory consistency of device performance achieved, we further assessed the stability of the devices. The steady-state output of the optimized devices was evaluated at the maximum power point (MPP) under standard conditions of 1-sun illumination and room temperature for 5 minutes. Notably, the steady-state output of the device remains stable over the test period, as evidenced by the consistent short-circuit current and PCE values (Fig. 4D). Another strong criterion for evaluating the stability of thin films and devices is the long-term operational lifetime under light-soaking and elevated temperatures. The photo-thermal stability of perovskite films, fabricated with varying dripping speeds, was examined by tracking the UV-Vis absorption spectra over time (Fig. S23, ESI†). Remarkably, all unsealed samples show negligible degradation after 2030 hours of aging at 65 °C in an N<sub>2</sub>-filled chamber under 1-sun metal-halide lamps. The devices were aged using the standard ISOS-L3 protocol, which involves maintaining the devices at 65 °C with the MPP tracking under continuous light exposure.<sup>53–55</sup> Considering the photo-thermal instability of spiro-OMeTAD and PEA<sup>+</sup> in FA<sup>+</sup>-containing perovskites,<sup>56</sup> here, we replaced them with more stable PDCBT and BCF-doped PTAA bilayer configuration for photo-thermal stability testing.<sup>53,57</sup> as shown in Fig. S24 (ESI†), the initial efficiency of the devices with the doped polymer bilayer was 21.2%, which is lower than the spiro-OMeTAD-based device. Given the thermal instability drawbacks of spiro-OMeTAD, future studies will be launched to discover thermally stable spiro-OMeTAD derivatives that can potentially match or exceed the efficiency. As shown in Fig. 4E and Fig. S25 (ESI†), the unsealed devices exhibit impressive stability behavior after continuous aging at 60–65 °C in a nitrogen-filled chamber under metal-halide lamps with an intensity of 83 mW cm<sup>-2</sup>. Specifically, the devices retained 93% ± 3% of their initial efficiency after 1200 hours. These findings not only validate the efficacy of enhancing device efficiency and durability through optimizing the fabrication process but also underscore the practical significance of optimized devices in real-world applications.

## Summary and outlook

In this report, we utilized a fully automated device acceleration platform (DAP) named SPINBOT to systematically optimize the

key parameters for the preparation of full perovskite devices in ambient air. Specifically, our study concentrated on analyzing the influence of the dripping speed of organic ammonium halide on perovskite films and devices. This involved a detailed examination of the relationship between processing conditions, structural characteristics, and device performance. Our findings indicate that moderate dropping speeds are critical for achieving high-performance devices. Conversely, excessively high or low speeds lead to performance degradation. Specifically, dripping speeds below 10 μL s<sup>-1</sup> can result in the formation of non-perovskite phases, adversely affecting the overall device efficiency. These findings evidence why the manual preparation of high-performance devices still relies heavily on the empirical manipulation and decision-making of human experts in a single laboratory, and why “optimization procedures” often suffer from intra-laboratory reproducibility and laboratory-to-laboratory reproducibility. As a result, the optimized parameter set enabled us to achieve perovskite devices with efficiencies exceeding 23% and satisfactory stability under ambient conditions. This work not only emphasizes the critical role of precise control and optimization of process parameters in improving perovskite device performance but also the necessity to introduce DAP-like automated platforms to accelerate the development of high-performance perovskite photovoltaics. More importantly, this study highlights the potential of preparing high-performance perovskite devices in the air through precise control of process parameters, even with no use of additives in perovskite formulation, which is of great significance for the commercialization and practical application of perovskite solar photovoltaics.

Looking to the future, we envision the establishment of an innovative and forward-thinking laboratory powered by Artificial Intelligence (AI), termed the Autonomous Material and Device Acceleration Platforms (AMADAP) laboratory, to further strengthen and universalize autonomous functional solar materials discovery and development as a prerequisite for developing digital twin models with inverse predictive power.<sup>58</sup>

## Data availability

The data supporting this article have been included in this article or as part of the ESI.†

## Author contributions

J. Z. and C. J. B. conceptualized the research project. J. Z. designed and performed the whole sample fabrication experiments. J. Z. and J. W. tested the perovskite thin films. A. B. performed SEM measurement. S. Q., J. Z., and T. D. performed *in situ* PL characterization. J. Z. and J. W. analyzed the device data. J. Z., Y. Z., Z. P., and T. H. carried out the device stability test. V. L. guided the optimization process. F. S. smoothed the automated platform. J. A. H. and C. J. B. supervised the project. J. Z. made the figures and wrote the manuscript. C. J. B. contributed mainly to the framework revision of the manuscript. J. W., T. D., S. Q., K. Z., and C. L. contributed to the





editing of the manuscript. All authors contributed to the discussion of experimental results and the manuscript.

## Conflicts of interest

The authors declare no competing interests.

## Acknowledgements

J. Z., J. A. H., and C. J. B. gratefully acknowledge the grants AutoPeroSol (ZT-I-PF-3-020) and AI-InSu-Pero (ZT-I-PF-5-106) by the Helmholtz Foundation. J. Z., K. Z., Z. P., J. T., CH. L., and C. L. gratefully acknowledge financial support from the China Scholarship Council (CSC). J. W. gratefully acknowledges financial support from the Sino-German Postdoc Scholarship Program (CSC-DAAD). C. L. gratefully acknowledges financial support from the Solar Tap (E1120206). J. A. H. and C. J. B. gratefully acknowledge the grants “ELF-PVDesign and development of solution processed functional materials for the next generations of PV technologies” (No. 44-6521a/20/4) by the Bavarian State Government. C. J. B. gratefully acknowledges financial support through the “Aufbruch Bayern” initiative of the state of Bavaria (EnCN and “Solar Factory of the Future”), the Bavarian Initiative “Solar Technologies go Hybrid” (SolTech), and the German Research Foundation (DFG) SFB 953-No. 182849149, and GRK2495 (ITRG2495).

## References

- J. Y. Kim, J.-W. Lee, H. S. Jung, H. Shin and N.-G. Park, *Chem. Rev.*, 2020, **120**, 7867–7918.
- H. J. Snaith, *Nat. Mater.*, 2018, **17**, 372–376.
- O. Almora, D. Baran, G. C. Bazan, C. Berger, C. I. Cabrera, K. R. Catchpole, S. Erten-Ela, F. Guo, J. Hauch and A. W. Ho-Baillie, *Adv. Energy Mater.*, 2021, **11**, 2002774.
- T. Wang, W. Deng, J. Cao and F. Yan, *Adv. Energy Mater.*, 2023, **13**, 2201436.
- F. Ma, Y. Zhao, Z. Qu and J. You, *Acc. Mater. Res.*, 2023, **4**, 716–725.
- J. Jeong, M. Kim, J. Seo, H. Lu, P. Ahlawat, A. Mishra, Y. Yang, M. A. Hope, F. T. Eickemeyer and M. Kim, *Nature*, 2021, **592**, 381–385.
- H. Min, D. Y. Lee, J. Kim, G. Kim, K. S. Lee, J. Kim, M. J. Paik, Y. K. Kim, K. S. Kim, M. G. Kim, T. J. Shin and S. Il Seok, *Nature*, 2021, **598**, 444–450.
- G. Wang, Q. Lian, D. Wang, F. Jiang, G. Mi, D. Li, Y. Huang, Y. Wang, X. Yao, R. Shi, C. Liao, J. Zheng, A. Ho-Baillie, A. Amini, B. Xu and C. Cheng, *Adv. Mater.*, 2022, **34**, 2205143.
- L. Yan, H. Huang, P. Cui, S. Du, Z. Lan, Y. Yang, S. Qu, X. Wang, Q. Zhang, B. Liu, X. Yue, X. Zhao, Y. Li, H. Li, J. Ji and M. Li, *Nat. Energy*, 2023, **8**, 1158–1167.
- Z. Liu, N. Rolston, A. C. Flick, T. W. Colburn, Z. Ren, R. H. Dauskardt and T. Buonassisi, *Joule*, 2022, **6**, 834–849.
- I. M. De Los Santos, H. J. Cortina-Marrero, M. Ruíz-Sánchez, L. Hechavarría-Difur, F. Sánchez-Rodríguez, M. Courel and H. Hu, *Sol. Energy*, 2020, **199**, 198–205.
- M. Awais, D. Thrithamarassery Gangadharan, F. Tan and M. I. Saidaminov, *Chem. Mater.*, 2022, **34**, 8112–8118.
- B. Cao, L. A. Adutwum, A. O. Oliynyk, E. J. Lubber, B. C. Olsen, A. Mar and J. M. Buriak, *ACS Nano*, 2018, **12**, 7434–7444.
- J. George and G. Hautier, *Trends Chem.*, 2021, **3**, 86–95.
- K. P. Goetz and Y. Vaynzof, *ACS Energy Lett.*, 2022, **7**, 1750–1757.
- J. Wagner, C. G. Berger, X. Du, T. Stubhan, J. A. Hauch and C. J. Brabec, *J. Mater. Sci.*, 2021, **56**, 16422–16446.
- N. J. Szymanski, B. Rendy, Y. Fei, R. E. Kumar, T. He, D. Milsted, M. J. McDermott, M. Gallant, E. D. Cubuk and A. Merchant, *Nature*, 2023, 1–6.
- X. Du, L. Lüer, T. Heumueller, J. Wagner, C. Berger, T. Osterrieder, J. Wortmann, S. Langner, U. Vongsaysy, M. Bertrand, N. Li, T. Stubhan, J. Hauch and C. J. Brabec, *Joule*, 2021, **5**, 495–506.
- D. P. Tabor, L. M. Roch, S. K. Saikin, C. Kreisbeck, D. Sheberla, J. H. Montoya, S. Dwaraknath, M. Aykol, C. Ortiz, H. Tribukait, C. Amador-Bedolla, C. J. Brabec, B. Maruyama, K. A. Persson and A. Aspuru-Guzik, *Nat. Rev. Mater.*, 2018, **3**, 5–20.
- T. C. Wu, A. Aguilar-Granda, K. Hotta, S. A. Yazdani, R. Pollice, J. Vestfrid, H. Hao, C. Lavigne, M. Seifrid, N. Angello, F. Bencheikh, J. E. Hein, M. Burke, C. Adachi and A. Aspuru-Guzik, *Adv. Mater.*, 2023, **35**, 2207070.
- J. Zhang, J. A. Hauch and C. J. Brabec, *Acc. Chem. Res.*, 2024, **57**, 1434–1445.
- T. Osterrieder, F. Schmitt, L. Lüer, J. Wagner, T. Heumueller, J. Hauch and C. J. Brabec, *Energy Environ. Sci.*, 2023, **16**, 3984–3993.
- B. P. MacLeod, F. G. Parlange, T. D. Morrissey, F. Häse, L. M. Roch, K. E. Dettelbach, R. Moreira, L. P. Yunker, M. B. Rooney and J. R. Deeth, *Sci. Adv.*, 2020, **6**, eaaz8867.
- M. Seifrid, R. Pollice, A. Aguilar-Granda, Z. Morgan Chan, K. Hotta, C. T. Ser, J. Vestfrid, T. C. Wu and A. Aspuru-Guzik, *Acc. Chem. Res.*, 2022, **55**, 2454–2466.
- Y. Shi, P. L. Prieto, T. Zepel, S. Grunert and J. E. Hein, *Acc. Chem. Res.*, 2021, **54**, 546–555.
- Q. Zhu, Y. Huang, D. Zhou, L. Zhao, L. Guo, R. Yang, Z. Sun, M. Luo, F. Zhang and H. Xiao, *Nat. Synth.*, 2023, 1–10.
- C. W. Coley, D. A. Thomas III, J. A. Lummiss, J. N. Jaworski, C. P. Breen, V. Schultz, T. Hart, J. S. Fishman, L. Rogers and H. Gao, *Science*, 2019, **365**, eaax1566.
- J. Wu, J. Zhang, M. Hu, P. Reiser, L. Torresi, P. Friederich, L. Lahn, O. Kasian, D. M. Guldi, M. E. Pérez-Ojeda, A. Barabash, J. S. Rocha-Ortiz, Y. Zhao, Z. Xie, J. Luo, Y. Wang, S. I. Seok, J. A. Hauch and C. J. Brabec, *J. Am. Chem. Soc.*, 2023, **145**, 16517–16525.
- M. Liu, K. Chen, D. Christian, T. Fatima, N. Pissarnitski, E. Streckfuss, C. Zhang, L. Xia, S. Borges and Z. Shi, *ACS Comb. Sci.*, 2012, **14**, 51–59.
- Y. Huang, R. U. Sheth, S. Zhao, L. A. Cohen, K. Dabaghi, T. Moody, Y. Sun, D. Ricaurte, M. Richardson, F. Velez-



- Cortes, T. Blazejewski, A. Kaufman, C. Ronda and H. H. Wang, *Nat. Biotechnol.*, 2023, **41**, 1424–1433.
- 31 W. Zeng, L. Guo, S. Xu, J. Chen and J. Zhou, *Trends Biotechnol.*, 2020, **38**, 888–906.
- 32 Y. Zhao, J. Zhang, Z. Xu, S. Sun, S. Langner, N. T. P. Hartono, T. Heumueller, Y. Hou, J. Elia, N. Li, G. J. Matt, X. Du, W. Meng, A. Osvet, K. Zhang, T. Stubhan, Y. Feng, J. Hauch, E. H. Sargent, T. Buonassisi and C. J. Brabec, *Nat. Commun.*, 2021, **12**, 1–9.
- 33 S. Sun, N. T. Hartono, Z. D. Ren, F. Oviedo, A. M. Buscemi, M. Layurova, D. X. Chen, T. Ogunfunmi, J. Thapa and S. Ramasamy, *Joule*, 2019, **3**, 1437–1451.
- 34 S. Chen, Y. Hou, H. Chen, X. Tang, S. Langner, N. Li, T. Stubhan, I. Levchuk, E. Gu, A. Osvet and C. J. Brabec, *Adv. Energy Mater.*, 2018, **8**, 1701543.
- 35 J. Zhang, J. Wu, S. Langner, B. Zhao, Z. Xie, J. A. Hauch, H. A. Afify, A. Barabash, J. Luo, M. Sytnyk, W. Meng, K. Zhang, C. Liu, A. Osvet, N. Li, M. Halik, W. Heiss, Y. Zhao and C. J. Brabec, *Adv. Funct. Mater.*, 2022, **32**, 2207101, DOI: [10.1002/adfm.202207101](https://doi.org/10.1002/adfm.202207101).
- 36 J. Yang, B. J. Lawrie, S. V. Kalinin and M. Ahmadi, *Adv. Energy Mater.*, 2023, 2302337, DOI: [10.1002/aenm.202302337](https://doi.org/10.1002/aenm.202302337).
- 37 H. S. Stein and J. M. Gregoire, *Chem. Sci.*, 2019, **10**, 9640–9649.
- 38 S. Li, H. Ren and Y. Yan, *Appl. Surf. Sci.*, 2019, **484**, 1191–1197.
- 39 J. Zhang, B. Liu, Z. Liu, J. Wu, S. Arnold, H. Shi, T. Osterrieder, J. A. Hauch, Z. Wu, J. Luo, J. Wagner, C. G. Berger, T. Stubhan, F. Schmitt, K. Zhang, M. Sytnyk, T. Heumueller, C. M. Sutter-Fella, I. M. Peters, Y. Zhao and C. J. Brabec, *Adv. Energy Mater.*, 2023, 2302594, DOI: [10.1002/aenm.202302594](https://doi.org/10.1002/aenm.202302594).
- 40 H. Tan, A. Jain, O. Voznyy, X. Lan, F. P. Garcia de Arquer, J. Z. Fan, R. Quintero-Bermudez, M. Yuan, B. Zhang and Y. Zhao, *Science*, 2017, **355**, 722–726.
- 41 N. J. Jeon, J. H. Noh, Y. C. Kim, W. S. Yang, S. Ryu and S. I. Seok, *Nat. Mater.*, 2014, **13**, 897–903.
- 42 W. S. Yang, J. H. Noh, N. J. Jeon, Y. C. Kim, S. Ryu, J. Seo and S. I. Seok, *Science*, 2015, **348**, 1234–1237.
- 43 Z. Ma, D. Huang, Q. Liu, G. Yan, Z. Xiao, D. Chen, J. Zhao, Y. Xiang, C. Peng and H. Li, *J. Energy Chem.*, 2022, **66**, 152–160.
- 44 L. Wang, C. McCleese, A. Kovalsky, Y. Zhao and C. Burda, *J. Am. Chem. Soc.*, 2014, **136**, 12205–12208.
- 45 Q. Chen, H. Zhou, T.-B. Song, S. Luo, Z. Hong, H.-S. Duan, L. Dou, Y. Liu and Y. Yang, *Nano Lett.*, 2014, **14**, 4158–4163.
- 46 Q. Jiang, Z. Chu, P. Wang, X. Yang, H. Liu, Y. Wang, Z. Yin, J. Wu, X. Zhang and J. You, *Adv. Mater.*, 2017, **29**, 1703852.
- 47 H. Zhang, W. Yu, J. Guo, C. Xu, Z. Ren, K. Liu, G. Yang, M. Qin, J. Huang, Z. Chen, Q. Liang, D. Shen, Z. Wu, Y. Zhang, H. T. Chandran, J. Hao, Y. Zhu, C.-s Lee, X. Lu, Z. Zheng, J. Huang and G. Li, *Adv. Energy Mater.*, 2022, **12**, 2201663.
- 48 B.-w Park, N. Kedem, M. Kulbak, D. Y. Lee, W. S. Yang, N. J. Jeon, J. Seo, G. Kim, K. J. Kim, T. J. Shin, G. Hodes, D. Cahen and S. I. Seok, *Nat. Commun.*, 2018, **9**, 3301.
- 49 J. Zhang, S. Langner, J. Wu, C. Kupfer, L. Lüer, W. Meng, B. Zhao, C. Liu, M. Daum, A. Osvet, N. Li, M. Halik, T. Stubhan, Y. Zhao, J. A. Hauch and C. J. Brabec, *ACS Energy Lett.*, 2022, **7**, 70–77.
- 50 S. Langner, F. Häse, J. D. Perea, T. Stubhan, J. Hauch, L. M. Roch, T. Heumueller, A. Aspuru-Guzik and C. J. Brabec, *Adv. Mater.*, 2020, **32**, 1907801.
- 51 J. Zhang, J. Wu, Y. Zhao, Y. Zou, A. Barabash, Z. Wu, K. Zhang, C. Deng, J. Elia, C. Li, J. S. Rocha-Ortiz, C. Liu, A. Saboor, I. M. Peters, J. A. Hauch and C. J. Brabec, *ACS Energy Lett.*, 2023, **8**, 3595–3603.
- 52 Q. Jiang, Y. Zhao, X. Zhang, X. Yang, Y. Chen, Z. Chu, Q. Ye, X. Li, Z. Yin and J. You, *Nat. Photonics*, 2019, **13**, 460–466.
- 53 Y. Zhao, T. Heumueller, J. Zhang, J. Luo, O. Kasian, S. Langner, C. Kupfer, B. Liu, Y. Zhong, J. Elia, A. Osvet, J. Wu, C. Liu, Z. Wan, C. Jia, N. Li, J. Hauch and C. J. Brabec, *Nat. Energy*, 2022, **7**, 144–152.
- 54 M. V. Khenkin, E. A. Katz, A. Abate, G. Bardizza, J. J. Berry, C. Brabec, F. Brunetti, V. Bulović, Q. Burlingame and A. Di Carlo, *Nat. Energy*, 2020, **5**, 35–49.
- 55 J. Luo, B. Liu, H. Yin, X. Zhou, M. Wu, H. Shi, J. Zhang, J. Elia, K. Zhang, J. Wu, Z. Xie, C. Liu, J. Yuan, Z. Wan, T. Heumueller, L. Lüer, E. Spiecker, N. Li, C. Jia, C. J. Brabec and Y. Zhao, *Nat. Commun.*, 2024, **15**, 2002.
- 56 M. Wang, Z. Shi, C. Fei, Z. J. D. Deng, G. Yang, S. P. Dunfield, D. P. Fenning and J. Huang, *Nat. Energy*, 2023, **8**, 1229–1239.
- 57 Y. Hou, X. Du, S. Scheiner, D. P. McMeekin, Z. Wang, N. Li, M. S. Killian, H. Chen, M. Richter, I. Levchuk, N. Schrenker, E. Spiecker, T. Stubhan, N. A. Luechinger, A. Hirsch, P. Schmuki, H.-P. Steinrück, R. H. Fink, M. Halik, H. J. Snaith and C. J. Brabec, *Science*, 2017, **358**, 1192–1197.
- 58 L. Lüer, I. M. Peters, V. M. L. Corre, K. Forberich, D. M. Guldi and C. J. Brabec, *Adv. Mater.*, 2024, **36**, 2308578.

